ROYAL SOCIETY
OF CHEMISTRY

PAPER

Check for updates

Unity fluorescent carbene–gold(I)–acetylide complexes with two-photon absorption and energy-efficient blue FOLEDs†

Alexander C. Brannan,[a] Hwan-Hee Cho, [iD] [b] Jonathan Daniel,[c] Amelia J. Harvey,[a] Charles T. Smith,[d] Nguyen Le Phuoc,[e] Mikko Linnolahti, [iD] *[e] Mireille Blanchard-Desce, [iD] *[c] Neil C. Greenham [iD] *[b] and Alexander S. Romanov [iD] *[a]

Two fluorescent organometallic "carbene–gold(I)–acetylide" (CMAc) complexes based on bicyclic alkyl-(amino) carbene (BIC), 4-ethynyl-2,1,3-benzothiadiazole (**Au1**) and 4,7-diethynyl-2,1,3-benzothiadiazole (**Au2**) have been synthesized and characterized. Compounds **Au1** and **Au2** exhibit blue to yellow fluorescence with up to unity fluorescence quantum yields and radiative rates exceeding 10^8 s^{-1}. The dipolar **Au1** complex exhibits a low two photon absorption cross-section (2PA σ_2) of 0.8 GM, whereas the quadrupolar **Au2** complex shows a high 2PA σ_2 value of 90 GM. A fluorescent CMAc organic light emitting diode (OLED) emits blue electroluminescence with up to 4.7% external quantum efficiency.

Introduction

Materials with third-order nonlinear optical (NLO) properties, for instance two-photon absorption (2PA) and two-photon excited fluorescence (2PF), has attracted ever-increasing interest from academia and industry due to their promising applications as materials for nano- or microfabrication and 3D-optical memory storage,[1] optical power limiting,[2] imaging and multiphoton microscopy,[3] and are particularly useful for biomedical applications such as photosensitizers for the photodynamic therapy of cancer[4] and many others. During the 2PA event, the molecule absorbs simultaneously two photons having the same polarization, while their photon's energy is equal to or slightly above half the energy gap between the ground and first excited states.[5] Therefore, 2PA molecular chromophores are characterized by the appearance of an absorption band at a lower

[a] *Department of Chemistry, The University of Manchester, Oxford Rd, Manchester M13 9PL, UK. E-mail: alexander.romanov@manchester.ac.uk*

[b] *Department of Physics, Cavendish Laboratory, Cambridge University, Cambridge, CB3 0HF, UK. E-mail: ncg11@cam.ac.uk*

[c] *Institut des Sciences Moléculaires (ISM, UMR5255), University of Bordeaux, Centre National de la Recherche Scientifique, Institut Polytechnique de Bordeaux, Bat A12, 351 Cours de la Libération, 33405 Talence, France. E-mail: mireille.blanchard-desce@u-bordeaux.fr*

[d] *Department of Physics and Astronomy and the Photon Science Institute, The University of Manchester, Oxford Road, Manchester, M13 9PL, UK*

[e] *Department of Chemistry, University of Eastern Finland, FI-80101 Joensuu, Finland. E-mail: mikko.linnolahti@uef.fi*

† Electronic supplementary information (ESI) available. CCDC 2351761. For ESI and crystallographic data in CIF or other electronic format see DOI: https://doi.org/10.1039/d4tc02845g

energy than the corresponding $S_0 \rightarrow S_1$ transition. The 2PA spectra exhibit a cross-section value, σ_2, measured in Göppert-Mayer (GM) units, where 1 GM equals 10^{-50} cm^4 s photon^{-1}. Large 2PA cross-sections (over 100 GM) and photochemical stability are highly sought-after characteristics to unlock the whole portfolio of advanced applications offered by 2PA materials. The best performing 2PA materials are commonly large macromolecules (conjugated polymers and Ru-containing dendrimers, σ_2 up to 10^4 GM),[6] while gold nanorods[7] are the champion inorganic materials with normalised σ_2 values up to 10^8 GM, albeit reported for solutions only. By contrast, small molecule organic and organometallic 2PA materials suffer from low σ_2 values ($<$1 GM) thus requiring a high laser power which may cause adverse effects in biomedical applications.

Such a striking difference between small and macromolecules suggests that efficient 2PA materials should exhibit a large change in polarization upon photoexcitation.[8] Therefore, the 2PA molecular design strategy pinpoints molecules with a large transition dipole moment ($\Delta\mu$, difference between ground and excited states).[9] Within the two-level approximation, the 2PA spectrum is represented by eqn (1):

$$\sigma_2(\nu) = B|\Delta\mu_{10}|^2|\mu_{10}|^2 g_2(\nu), \tag{1}$$

where B is another constant, $\Delta\mu_{10}$ is the difference between permanent dipole moments of the excited singlet (S_1) and ground (S_0) states, μ_{10} is the matrix element of the electronic transition dipole moment between states S_0 and S_1 and $g_2(\nu)$ is the 2PA line-shape function.[4b]

Various molecular designs have been proposed based on combinations between the donor (D) and acceptor (A) moieties,

This journal is © The Royal Society of Chemistry 2024

J. Mater. Chem. C, 2024, **12**, 13545–13554 | **13545**

connected with π-conjugated bridging units, to form extended π-conjugated systems to enhance the NLO properties of dipolar (D–π–A, D–π–D or A–π–A), quadrupolar (D–A–D or A–D–A), octupolar or even multipolar 2PA chromophores.[9] Among these molecular designs, small molecule organometallic alkynyl complexes of gold(ɪ), ruthenium(ɪɪ), and platinum(ɪɪ) demonstrated particularly strong 2PA cross-section values ranging from 10 to 10^4 GM, which is on par with those of organic macromolecules.[10] Late heavy transition metals (4d and 5d) appeared to be particularly beneficial due to their electron-rich nature and greater polarizability compared with 3d metal alkynyl complexes.[10] For instance, a common molecular design for neutral linear Au(ɪ)–complexes involves an alkynyl moiety with optionally-substituted fluorenyl benzothiazole (BTD) ligands, where the Au-atom possesses only 14 valence electrons (ve) and may only have one alkynyl ligand.[11] However, 2PA σ_2 values may be enhanced by coordination with strong σ-donor ligands, for instance phosphines or N-heterocyclic carbenes (NHC).[11] Such dipolar chromophores of the D-(Au)–A type gold complexes benefit from one-photon absorption (1PA) often happening in the UV-vis region, thus making them optically transparent for the desired applications in the visible wavelength range.[10,11] Several new linear (L)Au(ɪ)-complexes with directly coordinated 4-ethynylbenzothiadiazole (2PA-chromophores without a fluorenyl π-conjugated bridge) have been recently reported to have near unity fluorescence quantum yields with radiative rates of over 10^7 s^{-1}.[12] Regardless of such spectacular photophysical properties, there are no reports of their 2PA properties or tests of their performance in organic light-emitting diodes (OLEDs). Recently, we prepared a series of bright phosphorescent carbene–metal–acetylide (CMAc)[13] complexes with cyclic alkyl-(amino) carbene (CAAC) and cyclic alkyl(amino) carbene (BIC) ligands.[14] The BIC-carbene ligand is a strong σ-donor, which increases the electron density on the Au-atom. In addition, the BIC-carbene shows greater π-back bonding with the Au atom, thanks to the empty p_z-orbital on the carbene–carbon, thus providing greater delocalization of the electron density, making it a very promising building block for 2PA materials.

All these factors spurred our interest and motivated us to prepare new dipolar (**Au1**, Fig. 1) and quadrupolar (**Au2**) carbene–Au(ɪ)–acetylide (CMAc) materials, with a benzothiadiazole core, to reveal a principle advancement in the materials design strategy for efficient 2PA. We probe the effect of the superior electronic properties (σ-donor and π-acceptor) of the BIC-carbene on the 2PA efficiency, while investigating the applied potential of the title materials in OLED devices.

Results and discussion

Synthesis and structure

The ligands 4-ethynylbenzothiadiazole (**L1**) and 4,7-diethynyl-benzothiadiazole (**L2**) were prepared via Sonogashira cross-coupling between trimethylsilylacetylene and 4-bromo-2,1,3-benzothiadiazole or 4,7-dibromo-2,1,3-benzothiadiazole, respectively, followed by deprotection with tetra-N-butylammonium

Au1, dipolar D-Au-A 2PA chromophore
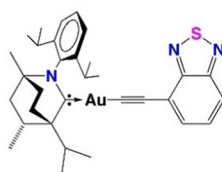
Au2, quadrupolar A-Au-D-Au-A 2PA chromophore
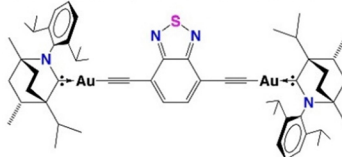
Fig. 1 Structures of new dipolar **Au1** and quadrupolar **Au2** carbene complexes and corresponding ligands **L1** and **L2**.

fluoride (TBAF). **L1** and **L2** were subsequently reacted with (BIC)AuCl under basic conditions to give carbene–metal–acetylide (CMAc) complexes **Au1** and **Au2**, respectively. Both complexes are yellow solids, soluble in polar and non-polar aprotic solvents such as dichloromethane (DCM), tetrahydrofuran (THF), toluene and methylcyclohexane (MCH). The complexes were fully characterised by NMR, IR, HRMS and elemental analysis. Both, **Au1** and **Au2** show good thermal stability with decomposition temperature T_d of 297 and 324 °C, respectively (Fig. S1, ESI†). The increase in thermal stability on increasing the number of (BIC)Au moieties concur with our previous work on gold(ɪ) alkynyl complexes of the type (BIC)Au(C≡CPh).[13c] **Au1** and **Au2** exhibit carbene resonances at 261.09 and 261.20 ppm in ^{13}C{1H} NMR which is similar to the previously reported 261.4 ppm for the (BIC)Au(C≡CPh) complex.[13c] BIC carbenes show greater σ-donating and π-accepting properties compared with NHC carbenes due to the absence of the second N atom adjacent to the carbene carbon. This results in the deshielding of ^{13}C-carbene compared to similar NHC complexes, for instance, (NHC)Au(ethynylBTD)[12] shows ^{13}C-carbene resonances in the range of 187–189 ppm (up to 75 ppm upfield shift compared to complexes **Au1** and **Au2** with BIC-carbene). The IR spectra show triple C≡C bond stretching vibrations at 2105 and 2107 cm^{-1} for **Au1** and **Au2**, which is ca. 12 cm^{-1} lower frequency compared to 2117 cm^{-1} for the (BIC)Au(C≡CPh) complex.[13c] This fact supports the stronger bonding of the ethynyl(BTD) ligand to the Au-atom that results in a weaker C≡C bond as a consequence of the lower C≡C bond frequency vibration compared to the (BIC)Au(C≡CPh) complex.

Cyclic voltammetry was performed for 1.4 mM THF solutions of **Au1** and **Au2** using a glassy carbon electrode and [n-Bu$_4$N]PF$_6$ as the supporting electrolyte (0.13 M) at a scan rate of 100 mV s^{-1} (Fig. 2, with data summarized in Table 1 and Table S1, ESI†). Both **Au1** and **Au2** show one quasi-reversible reduction with little variation in $E_{1/2}$ values at -2.0 ± 0.02 V. The peak-to-peak separation (ΔE_p) is 146 mV for **Au1** and **Au2** which is larger than the theoretical 59 mV value for the reversible redox process. The ratio between anodic and cathodic currents, $i_{pa}/i_{pc} = 0.9$ for both complexes, is close to unity for a fully reversible reduction process. **Au1** and **Au2** possess a

13546 | J. Mater. Chem. C, 2024, **12**, 13545–13554

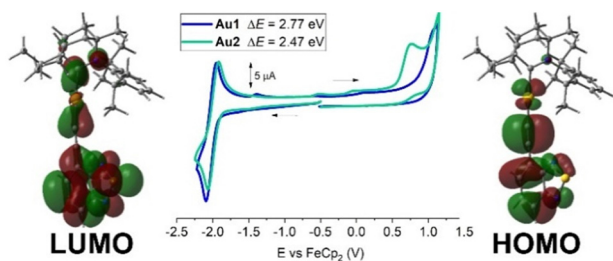This journal is © The Royal Society of Chemistry 2024

Fig. 2 Full range cyclic voltammograms for **Au1** and **Au2** with frontier molecular orbitals associated with the redox processes.

similar current peak value for the reduction process, suggesting a one-electron reduction process for both complexes. Collectively, the experimental data suggest a quasi-reversible character for the reduction event, consistent with the analogous NHC complexes.[12] We reported a similar (BIC)Au(C≡CPh) complex which shows a quasi-reversible reduction process at -2.90 ± 0.03 V and demonstrated that the LUMO is predominantly localised on the BIC carbene ligand.[13c] The 0.9 V difference in reduction potentials for **Au1**/**Au2** compared to this (BIC)Au(C≡CPh) complex suggests a much greater delocalization of the LUMO. The theoretical DFT calculations reveal that the LUMO is broadly delocalised over the ethynylBTD, gold and BiC ligands (Fig. 2 and Table S4, ESI†).

Both **Au1** and **Au2** show an irreversible oxidation process with no reduction back-peak (Fig. 2). The oxidation peak potential for **Au1** (+1.06 V) is 0.3 V anodically shifted compared to **Au2** (+0.76 V), suggesting an easier oxidation event for the π-extended and conjugated **Au2** complex, which indicates greater delocalization of the HOMO. Theoretical calculations confirm this (Fig. 2 and Table S4, ESI†) where the HOMO is exclusively localised over the Au(ethynylBTD) moiety. Analogous NHC complexes[12] were demonstrated to have similar trends and characteristics for the frontier orbitals. The calculations also indicate that there is only a 3–5% contribution of the gold atom to the HOMO and LUMO, suggesting that the redox events are predominantly localised on the BIC and ethynylBTD ligands. The energies of the HOMO and LUMO for **Au1** and **Au2** were estimated from the onset potential values for oxidation and reduction processes, see Table 1.

Single crystals for X-ray diffraction study were obtained by layer diffusion of hexane into DCM solution of **Au1** at room temperature. The molecular structure of **Au1** is shown in Fig. 3. Unlike analogous (NHC)Au(ethynylBTD) complexes with short aurophilic interactions,[12] **Au1** is monomeric with no Au···Au intermolecular interactions. The **Au1** molecules are arranged in a 3D-network via weak C–H···S and C–H···N intermolecular hydrogen bonds between BIC-carbene and BTD-ethynyl moieties. Complex **Au1** exhibits a near linear geometry around the gold atom with a C1–Au–C25 angle of 175.7(4)°, whereas the Au–C≡C moiety experiences a ca. 16° bending distortion, with an Au1–C25–C26 angle of 164.4°. The torsion angle between the BIC and BTD ligand planes is 69.4(2)°, demonstrating a highly twisted geometry between the donor and the acceptor. The gold–carbene(C1) bond length is closely similar to that in analogous (NHC)Au(ethynylBTD) complexes[12] whereas the gold–acetylide(C25) bond length of **Au1** is longer by ca. 0.07 Å. Such a strong deviation is likely due to static disorder of the ethynylBTD moiety which limits detailed discussion of the **Au1** structure.

Photophysical properties and theoretical considerations

The UV-visible absorption spectra (UV-vis) for complexes **Au1** and **Au2** (Fig. 4(a), (d) and Table 1) show well-resolved and high-energy absorption bands up to 340 nm for **Au1** and 375 nm for **Au2**. These are assigned to π–π* transitions for the core ethynylBTD ligand based on the high extinction coefficients ($\varepsilon > 1 \times 10^4$ M^{-1} cm^{-1}). Both, **Au1** and **Au2** exhibit a broad unstructured lower-energy absorption band, which suggests a charge transfer (CT) character of this transition. The CT-band for **Au2** experiences a 52 nm red-shift compared with **Au1** which is associated with greater π-delocalization for **Au2**. Complexes **Au1** and **Au2** display a weak negative solvatochromism for the CT-band, i.e. up to 12 nm blue-shift upon increasing solvent polarity (Fig. 4(a) and (d)). The extinction coefficients of **Au2** for the CT band (Table 1) are twice as high as those of **Au1**, indicating a higher degree of allowedness for the CT transition with a greater number of (BIC)Au moieties. This correlates with the two-fold higher oscillator strength coefficient for **Au2** ($f = 0.9733$, Table S6, ESI†) compared with **Au1** ($f = 0.3963$). Comparison of the UV-vis spectra of the unmetallated ligands

Table 1 Photophysical properties of gold complexes **Au1** and **Au2** in toluene solution and in 1%-doped Zeonex films at 298 and 77 K, UV-vis spectra in toluene solution, redox potentials (V), HOMO and LUMO energy levels, and 2PA characteristics

	λ_{em} (nm)	τ (ns, 295 K)	Φ_{PL} (%)	$k_r{}^c$ (10^7 s^{-1})	$k_{nr}{}^d$ (10^7 s^{-1})	$S_1{}^e$ (eV)	λ_{em} (nm) (τ, ns) 77 K	λ_{abs}, (nm)^f (ε/M^{-1} cm^{-1})	E_{red}, (V)	LUMO (eV)	E_{ox}, (V)	HOMO (eV)	λ^{2PA} (nm)	σ_2, (GM)
Toluene solution														
Au1	458	10.1	>99^a	9.8	0.01	3.00	440 (8.2)	391 (5070)	−2.02	−3.46	+1.06	−6.23	800	0.8
Au2	516	7.9	>99^a	12.5	0.01	2.87	483 (6.9)	356 (7680)	−1.99	−3.48	+0.76	−5.95	720	90
								445 (12 300)					820	2
1 wt% Zeonex Film														
Au1	460	9.4	81^b	8.6	2.2	2.98	461 (9.2)	—	—	—	—	—	—	—
Au2	534	6.1	52^b	8.5	7.9	2.58	529 (5.7)	—	—	—	—	—	—	—

^{a} Luminescence quantum yield measured with fluorescein in NaOH$_{aq.}$ (0.1 M, $\Phi_{PL} = 0.9$) as a reference. ^{b} Quantum yields determined using an integrating sphere. ^{c} Radiative rate constant $k_r = \Phi/\tau$. ^{d} Nonradiative constant $k_{nr} = (1 - \Phi)/\tau$. ^{e} Singlet energy levels based on the onset of the emission spectra blue edge at 77 K in MCH. ^{f} UV-vis for CMAc solution in methycyclohexane.
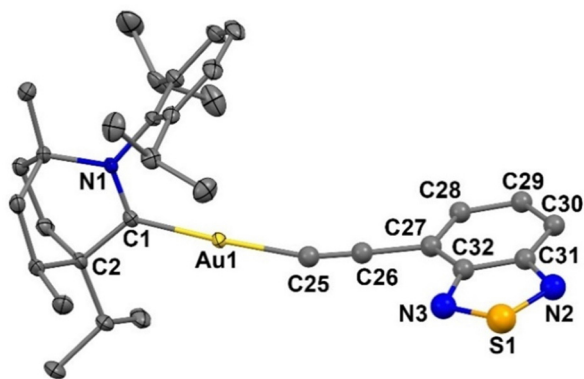
Fig. 3 Crystal structure of complex **Au1**. Ellipsoids are shown at the 50% probability level. Hydrogen atoms are omitted for clarity. Selected bond lengths (Å) an angles (°): complex 7: Au–C1 2.020(4), Au–C25 2.073(12), C1–N1 1.308(6), C25–C26 1.188(17), N2–S1 1.552(13), N3–S1 1.653(14), C1–Au–C25 175.7(4)°, **Au1**–C25–C26 164.4°, and C1–N1···C27–C28 69.4(2)°.

L1 and **L2** (Fig. S3, ESI†) with their aurated complexes **Au1** and **Au2** reveals over 50 nm red-shift for the CT band upon coordination of the BIC-gold moiety to **L1** and **L2**. Analogous phosphine and NHC-carbene gold complexes show similar red-shifts of their CT bands,[12e] which is due to an increase in conjugation and mixing of the 5d orbitals of the Au(I) centre with the π-system of the ethynylBTD ligand.[12,15] The optical energy gap for **Au1** (2.85 eV) and **Au2** (2.49 eV) was calculated from the onset of the red edge of the CT band in the THF absorption spectrum. It is fully consistent with the electronic energy gap measured by cyclic voltammetry in THF solution for **Au1** (2.77 eV) and **Au2** (2.47 eV). This suggests that CT

transition is predominantly HOMO → LUMO in nature. Our theoretical calculations suggest that the vertical $S_0 \rightarrow S_1$ transitions (Table S6, ESI†) are 94% and 91% HOMO → LUMO for **Au1** and **Au2**, respectively.

The photoluminescence (PL) spectra of **Au1** and **Au2** were measured in various solvents and 1%-doped Zeonex films at 298 and 77 K (Table 1 and Fig. 4, Fig. S4–S6, ESI†). Both complexes show broad, unstructured emission profiles in all media with positive solvatochromism in solutions (up to 25 nm red-shift MCH to DCM, Fig. 4(b) and (e)). This suggests a CT character of the emissive excited state. All complexes possess fast fluorescence excited state lifetimes in the range of 8–12 ns in all media (Table 1). These increase slightly with increasing solvent polarity (Fig. 4(b) and (e)). Both **Au1** and **Au2** show near-unity PL quantum yields (PLQY) in MCH and toluene solutions. Such bright and fast fluorescence results in radiative rates exceeding 1×10^8 s^{-1} (Table 1) for **Au1** and **Au2**. This experimental fact parallels the theoretical calculations which predict high oscillator strength coefficients (Tables S6, ESI†) for both complexes, *vide supra*.

On cooling to 77 K, Zeonex films of **Au1** and **Au2** show nearly identical photophysical characteristics to those measured at 295 K. However, in frozen MCH glass **Au1** and **Au2** show a blue-shift of the emission peak of up to 30 nm (Fig. S5, ESI†). We did not detect phosphorescence or delayed emission in all media at 77 K. All these facts confirm a fluorescence emission mechanism for the complexes **Au1** and **Au2**. Analogous (NHC)Au(ethynylBTD)[12] complexes show similar PL performance in solution: green or yellow near-unity fluorescence with up to 11 ns excited state lifetime, albeit with much greater variations for PLQY values in Zeonex films (31–83%).
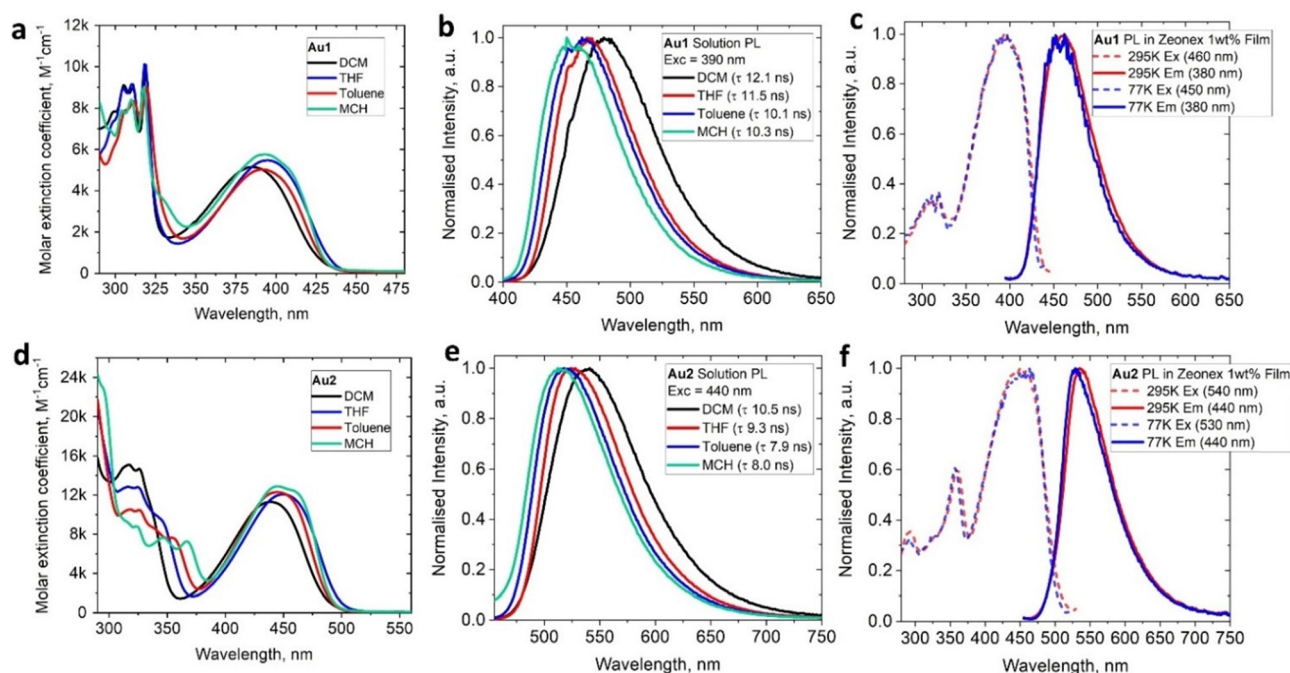

Fig. 4 UV-vis spectra in various solvents for **Au1** (a) and **Au2** (d); emission spectra in various solvents for **Au1** (b) and **Au2** (e); emission (solid lines) and excitation (dashed line) spectra of **Au1** (c) and **Au2** (f) in Zeonex matrices with 1 wt% dopant at 298 K and 77 K.

13548 | *J. Mater. Chem. C*, 2024, **12**, 13545–13554

This journal is © The Royal Society of Chemistry 2024

Theoretical calculations were performed for complexes **Au1** and **Au2** to reveal the non-emissive (dark) triplet excited state. The first triplet excited state T_1 possesses HONTO and LUNTO orbitals predominantly localised over the ethynylBTD ligand (Tables S6 and S7, ESI†). Therefore, we ascribe a locally excited (^{3}LE) character to the T_1-state. It has a large HOMO/LUMO overlap integral that stabilizes the T_1 state energy by *ca.* 1 eV for **Au1** and 2 eV for **Au2** compared to the S_1 state energy. We calculate the spin–orbit coupling matrix elements (SOCME, Tables S8 and S9, ESI†) between the triplet and singlet excited states for **Au1** and **Au2** to support a very weak coupling between S_1 and T_1 states. This suggests a weak intersystem crossing (ISC), *i.e.* no phosphorescence for **Au1** and **Au2**, consistent with the previous reports on fluorescent gold alkynyl complexes.[12]

Fluorescence from **Au1** and **Au2** is in stark contrast with our previously reported phosphorescent (BIC)Au(C≡CPh) complex having only *ca.* 0.6 eV energy difference between S_1 and T_1 states. Unlike **Au1** and **Au2**, this complex emits fast prompt fluorescence from a high lying CT state and a dominant phosphorescence from the ^{3}LE excited state localised at the phenylacetylide ligand thanks to high contribution of the gold orbitals (*ca.* 16%) and fast ISC rate of 9 ps.[13c] Collectively, the small contribution of the gold orbitals to HOMO and LUMO (3–5%) and the large energy gap between the S_1 and T_1 states for **Au1** and **Au2** suggests an inefficient ISC, thus explaining the dark nature of the T_1 state.

Two-photon absorption (2PA) studies. We measured 2PA spectra and cross sections (σ_2) for complexes **Au1** and **Au2** and ligands **L1** and **L2** in deaerated toluene solutions to evaluate the auration effect on 2PA efficiency of small molecule chromophores. The dipolar chromophore **Au1** may particularly benefit from the relaxation of the parity selection rules for 1PA and 2PA transitions for noncentrosymmetric molecules.[4b] Thanks to the fluorescence properties of **Au1** and **Au2**, the 2PA spectra were measured using two-photon excited fluorescence (TPEF) technique. The solutions were excited by a tunable femto-second Ti:sapphire oscillator system (pulse duration 150 fs, 80 MHz repetition rate) on the full 2PA range (*ca.* 680–1000 nm) and data are presented in Fig. 5 and Table 1. 1PA and 2PA spectra are shown in the same plot for comparison, see Fig. 5(a) and (d). Ligands **L1** and **L2** have a small 2PA cross section $\sigma_2 \approx 1$ and 23 GM in the 680–880 nm region. The 2PA spectra of the dipolar chromophore **Au1** show a well-defined peak in the same region of 680–880 nm with a small σ_2 value of 0.8 GM, similar to that for **L1**. Compared to dipolar **Au1**, the quadrupolar chromophore **Au2** demonstrates 100-fold higher 2PA σ_2 values approaching 90 GM at 720 nm wavelength. This is also a four-fold increase compared with ligand **L2**, thus clearly demonstrating a strong enhancement of the 2PA upon auration. Various similar gold(I) complexes with large conjugated and π-extended molecular design demonstrated 2PA values of up to 150 GM.[11b] Therefore, we demonstrate that it is not always necessary to synthesize complicated π-extended molecular systems while the quadrupolar molecular design with advanced ligands, for instance CAAC-carbenes, enables high performance even for small molecule 2PA chromophores, such as complex **Au2**. One of the main factors that influence 2PA is the transition dipole moment from the ground to the first excited state, $\Delta\boldsymbol{\mu}_{10}$.[4b] Both **Au1** and **Au2** complexes show a similar $\Delta\boldsymbol{\mu}_{10}$
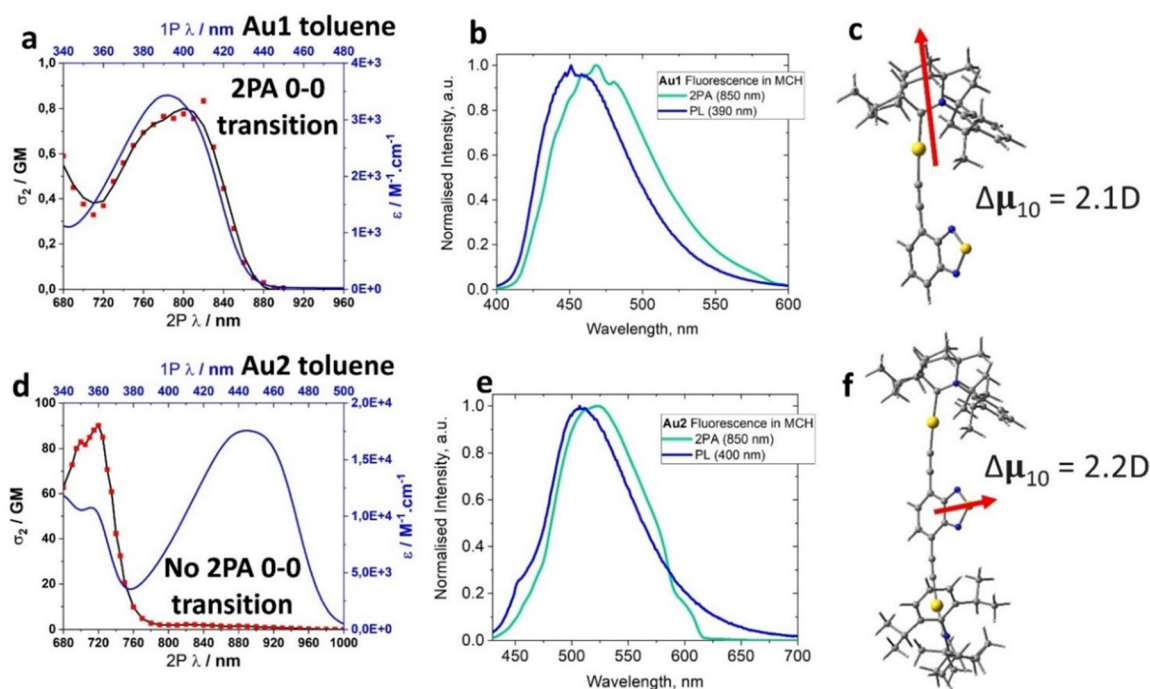

Fig. 5 Two-photon cross-section (red: experimental, black: smooth) and molar extinction of complexes **Au1** (a) and **Au2** (d) in toluene saturated with argon (blue). Overlay of the one-photon fluorescence (blue) and two-photon fluorescence (green) for complexes **Au1** (b) and **Au2** (e) in MCH solution under argon. Optimized molecular structure of complexes **Au1** (c) and **Au2** (f) with orientation and value for the transition dipole moment, $\Delta\boldsymbol{\mu}_{10}$.

value of *ca.* 2 Debye. The orientation of the transition dipole moment for **Au1** and **Au2** is essentially orthogonal to each other, *i.e.* **Au1** shows a vector parallel the longest axis of the molecules whereas the **Au2** complex has a vector perpendicular to the longest axis of the molecule, see Fig. 5(c) and (f). This is likely connected with superior 2PA σ_2 values for the **Au2** complex. The two-photon excited fluorescence spectra are shown in Fig. 5(b) and (e), where the 2PA PL profile (blue) is slightly red-shifted compared to 1PA PL (cyan). This phenomenon has previously been observed and explained due to certain vibronic transitions to becoming more enhanced in the 2PA process,[4b] whereas the pure electronic transition is the strongest in the one-photon process. The 2PA luminescence intensity *vs.* excitation-power log–log plots

show a gradient of two for both **Au1** and **Au2** (Fig. S7, ESI†), thus confirming that excitation occurs *via* a 2PA event.

OLED fabrication. The high thermal stability, volatility and superior photophysical characteristics of **Au1** encouraged us to fabricate vapour-deposited OLED devices. We test the hypothesis that 2PA chromophores may be suitable in the construction of OLEDs operating *via* a triplet–triplet annihilation process (TTA, Fig. 6(h)). This is due to the significantly stabilised T_1 energy for **Au1** which is close to one-half of the singlet excited state S_1 energy, unity blue fluorescence PLQY and high radiative rate exceeding 1×10^8 s^{-1} which are the major preconditions to enable the TTA process.[16] The TTA process also requires a high concentration of long-lived triplet excited
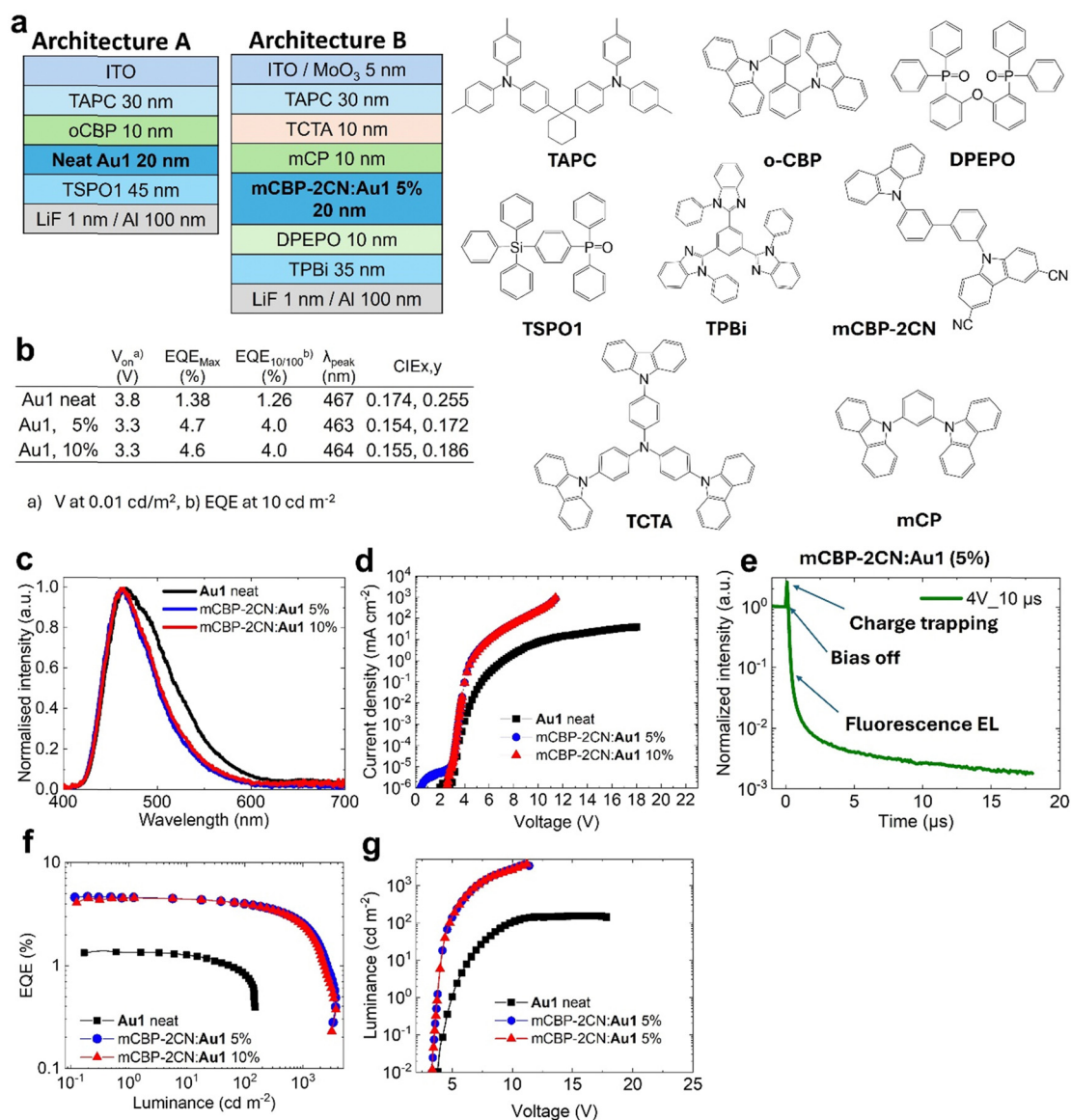

Fig. 6 Vapor-deposited OLED device architectures. (a) OLED architectures A for neat **Au1** and B for **Au1** doped with *m*CBP-2CN at 5 and 10% by weight and chemical structures of the materials used; (b) performance data of vapor-deposited **Au1** OLED; (c) normalised electroluminescence spectra from devices incorporating **Au1** neat and in host–guest structures; (d) current density–voltage plot; (e) transient electroluminescence profiles for **Au1** in *m*CBP-2CN at 5% by weight showing strong prompt fluorescence and weak phosphorescence profile after 1 μs delay; (f) EQE *versus* luminance plot; (g) luminance–voltage plot; and (h) excited state energy diagram for complex **Au1** with radiative EL pathways.

13550 | *J. Mater. Chem. C*, 2024, **12**, 13545–13554

This journal is © The Royal Society of Chemistry 2024

states because of its bimolecular nature.[16] To satisfy the latter criterion, a host-free OLED device (architecture A, Fig. 6(a)) was fabricated following the structure: ITO/TAPC (30 nm)/*o*-CBP (10 nm)/neat **Au1** (20 nm)/TSPO1 (45 nm)/LiF (1 nm)/Al (100 nm). The best OLED device shows a sky-blue electroluminescence (EL, λ_{max} = 467 nm, Fig. 6(b)) with a maximum external quantum efficiency (EQE) of 1.3%. We explain the low efficiency of the neat **Au1** OLED with additional requirements such as $\pi\cdots\pi$ stacking interactions between the molecules, which was not observed in the packing of the **Au1** molecules in the unit cell of the single crystal, *vide supra*.

To enhance the performance of **Au1** in OLED by increasing the probability of $\pi\cdots\pi$ stacking interactions, we attempted to prepare a host–guest OLED devices where **Au1** was co-evaporated with the *m*CBP-2CN host at 5 and 10% concentration as shown in Fig. 6(a) (architecture B). *m*CBP-2CN is an ambipolar host with a high triplet energy of 2.77 eV and a well-stabilised HOMO energy level (−6.1 eV), which gives an acceptable energy alignment for complex **Au1**.[17] Electroluminescence (EL) spectra for 5 and 10% **Au1** OLED devices are shown in Fig. 6. The EL profile peaks at λ_{max} = 467 nm perfectly matching with the fluorescence PL profile of complex **Au1**. The EL profile of the host–guest OLEDs is slightly narrower compared to the neat OLED, thus explaining the more blue CIE colour space coordinates for the former (0.15, 0.17, see Fig. 6(b)). Host–guest OLED devices show a low turn-on voltage down to V_{On} = 3.3 ± 0.3V (when luminance equals 0.1 cd m^{-2} at the applied bias). Fig. 6 shows the current density–voltage, luminance–voltage, EQE *versus* luminance plots for the best blue **Au1** OLED in a host–guest environments. The OLEDs demonstrate a four-fold increase in peak EQEs of up to 4.7% compared to the host-free **Au1** OLED. The **Au1** devices experience a small EQE efficiency roll-off to 4% at a practical brightness of 100 cd m^{-2}.

We measured the transient-EL for the *m*CBP-2CN:**Au1**(5%) OLED device (Fig. 6(e)) to reveal the role of the triplet state and the delayed-fluorescent component in OLEDs. The EL shows a biexponential decay with up to 10 ns fluorescence and microsecond delayed fluorescence in the OLED device held at a practical brightness of 100 cd m^{-2}. However, the transient electroluminescence trace (Fig. 6(e)) shows a clear spike after "bias-off" which is characteristic of the delayed electroluminescence originating from the recombination of trapped charge carriers. Therefore, the similarity between PL and EL profiles with a dominant nanosecond range kinetics suggests the fluorescence electroluminescence in the OLED device.

Conclusions

We demonstrated a molecular design strategy towards thermally stable gold carbene–metal(ɪ)–acetylide (CMAc) materials with unity fluorescence and high radiative rates exceeding 1×10^8 s^{-1}. The bulky nature of the BIC-carbene ligand prevents aggregation in the solid state. Cyclic voltammetry data show that the redox processes for **Au1** and **Au2** are largely localised over the ethynyl-benzothiazole (ethynylBTD) ligand, resulting in greater stabilization of the HOMO energy levels

down to −6.23 eV for **Au2** due to greater π-conjugation. Absorption spectra and theoretical calculations confirm that the lowest energy vertical transition has over 90% HOMO → LUMO charge transfer (CT) character. Both **Au1** and **Au2** show a large HOMO/LUMO overlap integral (0.69) resulting in a significant stabilisation of the triplet excited state T_1 energy. The low contribution of the gold atom (up to 5%) in the HOMO and LUMO coupled with a weak spin–orbit coupling between S_1 and T_1 states suggests a weak ISC process for **Au1** and **Au2**, which explains the exclusive and bright fluorescence. We demonstrate an auration effect to enhance the two-photon absorption cross-sections (2PA σ_2) for the quadrupolar chromophore **Au2** (90 GM), *i.e.* a four-fold increase compared with the starting organic ligand **L2** (23 GM) and a 100-fold increase compared to the dipolar chromophore **Au1** (0.8 GM). The mutual orthogonality of the transition dipole vector between **Au1** and **Au2** is likely responsible for such a stark difference in 2PA σ_2 values. Proof-of-concept fluorescent OLED devices have been fabricated with a maximum EQE of 4.7% approaching the theoretical maximum EQE of 5% thus indicating the excellent performance of the **Au1** complex under electrical excitation. Overall, this work directs future CMAc material design to use ancillary carbene ligands with superior electronic properties (CAAC and BIC-carbenes) and π-conjugated alkynyl ligands to obtain quadrupolar type chromophores with large 2PA absorption cross-sections, bright 2PEF and energy-efficient CMAc OLEDs.

Experimental section

General considerations

All reactions were performed under a N$_2$ atmosphere. Solvents were dried as required. Reagents and catalysts were purchased from commercial vendors and used as received. (BIC)AuCl^{14b,c} was prepared according to the literature procedure, see the ESI.† Synthetic procedures for **L1** and **L2** are found in the ESI.† ^{1}H and ^{13}C$\{^1$H$\}$ NMR spectra were recorded using a Bruker AVIII HD 500 MHz NMR spectrometer. ^{1}H NMR spectra (500.19 MHz) and ^{13}C$\{^1$H$\}$ (125.79 MHz) were referenced to CD$_2$Cl$_2$ at δ 5.32 (^{13}C, δ 53.84) and CDCl$_3$ at δ 7.26 (^{13}C, δ 77.16). IR spectra were recorded using a Bruker ALPHA FT-IR spectrometer equipped with a platinum ATR attachment. All electrochemical experiments were performed using an Autolab PGSTAT 302N computer-controlled potentiostat. Cyclic voltammetry (CV) was performed using a three-electrode configuration consisting of a glassy carbon macrodisk working electrode (GCE) (diameter of 3 mm; BASi, Indiana, USA) combined with a Pt wire counter electrode (99.99%; GoodFellow, Cambridge, UK) and an Ag wire pseudoreference electrode (99.99%; Good-Fellow, Cambridge, UK). The GCE was polished between experiments using alumina slurry (0.3 μm), rinsed in distilled water and subjected to brief sonication to remove any adhering alumina microparticles. The metal electrodes were then dried in an oven at 100 °C to remove residual traces of water, the GCE was left to air dry and residual traces of water were removed

This journal is © The Royal Society of Chemistry 2024

J. Mater. Chem. C, 2024, **12**, 13545–13554 | **13551**

under vacuum. The Ag wire pseudoreference electrodes were calibrated to the ferrocene/ferrocenium couple in THF at the end of each run to allow for any drift in potential, following IUPAC recommendations. All electrochemical measurements were performed at ambient temperatures under an inert N_2 atmosphere in THF containing the complex under study (1.4 mM) and the supporting electrolyte [n-Bu$_4$N][PF$_6$] (0.13 M). Data were recorded using Autolab NOVA software (v. 1.11). Thermogravimetric analysis and elemental analyses were performed by the Microanalysis Laboratory at the University of Manchester. Mass spectrometry data were obtained by the Mass Spectrometry Laboratory at the University of Manchester. Thermogravimetric analysis was performed with a TA Instruments SDT650 simultaneous thermal analyser under a stream of nitrogen.

Synthesis of Au1. A Schlenk flask was charged with (BIC)AuCl (357 mg, 624 μmol) and KOtBu (77.1 mg, 687 μmol) followed by the addition of dry THF (15 mL). **L1** (100 mg, 624 μmol) was dissolved in dry THF (15 mL) and the solution was added to the reaction mixture at −78 °C dropwise. The solution was allowed to reach room temperature and left to stir overnight. Volatiles were removed under vacuum and the crude product was purified by column chromatography (eluent 4:1 hexane: EtOAc) to give the pure product as a pale green crystalline solid in 64% yield (279 mg, 402 μmol). ^{1}H NMR (500 MHz, CD$_2$Cl$_2$) δ 7.74 (d, J = 8.7 Hz, 1H, CH BTD), 7.52–7.46 (m, 2H, p-CH Dipp BIC and CH BTD), 7.43 (dd, J = 8.6, 7.1 Hz, 1H, CH BTD), 7.35–7.31 (m, 2H, m-CH Dipp BIC), 3.24–3.15 (m, 1H, CH iPr BIC), 3.07–2.98 (m, 1H, CH iPr Dipp BIC), 2.65–2.56 (m, 1H, CH iPr Dipp BIC), 2.31–2.22 (m, 1H, CH(CH$_3$) BIC), 2.13 (dd, J = 13.6, 10.5 Hz, 1H, CH BiCAAC), 1.84–1.70 (m, 3H, CH BIC), 1.64–1.58 (m, 1H, CH BIC), 1.56–1.52 (m, 1H, CH BIC overlap with water), 1.50–1.46 (m, 6H, 2xCH$_3$ iPr Dipp BIC), 1.41 (d, J = 6.7 Hz, 3H, iPr Dipp BIC), 1.35 (d, J = 6.9 Hz, 3H, iPr Dipp BIC), 1.29 (d, J = 6.9 Hz, 3H, CH$_3$ iPr BIC), 1.08 (t, J = 7.2 Hz, 6H, CH(CH$_3$) BIC and iPrCH$_3$ BIC), 1.02 (s, 3H, CH$_3$ BIC). ^{13}C NMR (126 MHz, CD$_2$Cl$_2$) δ 261.09 (C: BIC), 156.12 (C = N BTD), 155.14 (C = N BTD), 145.08 (o-C Dipp BIC), 144.43 (o-C Dipp BIC), 141.21 (i-C Dipp BIC), 139.17 (BTD), 132.15 (BTD), 129.88 (BTD), 129.85 (p-C Dipp BIC), 125.27 (m-C Dipp BIC), 120.39 (BTD), 119.38 (m-C Dipp BIC), 115.40 (C ≡ C), 101.74 (C≡C), 64.44 (C$_q$CH$_3$ BIC), 55.90 (C$_q$iPr BIC), 44.60 (CH(CH$_3$)CH$_2$ BIC), 34.61 (CH(CH$_3$) BIC), 32.89 (CH$_2$CH$_2$ BIC), 31.72 (CH iPr BIC), 29.49 (CH iPr Dipp), 28.89 (CH iPr Dipp), 25.61 (CH$_3$ iPr carbene), 25.39 (CH$_3$ iPr Dipp), 24.05 (C$_q$CH$_3$ carbene), 23.73 (CH$_3$ iPr Dipp), 23.40 (CH$_3$ iPr Dipp), 21.56 (CH BIC), 20.32 (CH$_2$CH$_2$ BIC), 19.69 (CH(CH$_3$) BIC), 16.23 (CH$_3$ iPr BIC). IR (ATR, cm^{-1}): 2105 (C≡C). Anal. calcd for C$_{32}$H$_{40}$AuN$_3$S: C, 55.25; H, 5.80; N, 6.04; S, 4.61; found = C, 53.83; H, 6.46; N, 4.81; S, 3.02. HRMS C$_{32}$H$_{40}$AuN$_3$S theoretical [M − H]$^+$ = 696.2681, HMRS APCI(ASAP) = 696. 2680. TGA C$_{32}$H$_{40}$AuN$_3$S T_d = 197.2 °C.

Synthesis of Au2. A Schlenk flask was charged with (BIC)AuCl (373 mg, 651 μmol) and KOtBu (80.4 mg, 717 μmol) followed by the addition of dry THF (15 mL). **L2** (60.0 mg, 326 μmol) was dissolved in THF (15 mL) and the solution was added to the reaction mixture at −78 °C dropwise. The solution was allowed to reach room temperature and left to stir overnight.

Volatiles were removed under vacuum and the crude product was purified by column chromatography (eluent 4:1 hexane: EtOAc) to give the pure product as a yellow powder in 55% yield (224 mg, 179 μmol). ^{1}H NMR (500 MHz, CD$_2$Cl$_2$) δ 7.51–7.42 (m, 2H, BTD), 7.35–7.24 (m, 6H, Dipp BIC), 3.22–3.11 (m, 2H, CH iPr BIC), 3.04–2.93 (m, 2H, CH iPr Dipp BIC), 2.62–2.52 (m, 2H, CH iPr Dipp BIC), 2.30–2.19 (m, 2H, CH(CH$_3$) BIC), 2.15–2.05 (m, 2H, CH BIC), 1.84–1.67 (m, 8H, CH BIC), 1.62–1.50 (2H, CH BIC overlap with water), 1.49–1.41 (m, 12H, iPr Dipp BIC), 1.40–1.22 (m, 18H, 12H iPr Dipp BIC and 6H CH$_3$ iPr BIC), 1.09–0.96 (m, 18H, 6H CH(CH$_3$) BIC, 6H iPrCH$_3$ BIC and 6H CH$_3$ BIC). ^{13}C NMR (126 MHz, CD$_2$Cl$_2$) δ 261.20 (C: BIC), 155.84 (C=N BTD), 145.04 (o-C Dipp BIC), 144.41 (o-C Dipp BIC), 141.19 (i-C Dipp BIC), 139.55 (BTD), 132.44 (BTD), 129.83 (p-C Dipp BIC), 125.26 (m-C Dipp BIC), 125.16 (m-C Dipp BIC), 117.90 (C≡C), 102.38 (C≡C), 64.35 (C$_q$CH$_3$ BIC), 55.86 (C$_q$iPr BIC), 44.60 (CH(CH$_3$)CH$_2$ BIC), 34.59 (CH(CH$_3$) BIC), 32.89 (CH$_2$CH$_2$ BIC), 31.69 (CH iPr BIC), 29.47 (CH iPr Dipp), 28.87 (CH iPr Dipp), 25.98 (CH$_3$ iPr Carbene), 25.59 (CH$_3$ iPr Dipp), 24.05 (C$_q$CH$_3$ Carbene), 23.72 (CH$_3$ iPr Dipp), 23.40 (CH$_3$ iPr Dipp), 21.55 (CH BIC), 20.30 (CH$_2$CH$_2$ BIC), 19.68 (CH(CH$_3$) BIC), 19.64, 16.22 (CH$_3$ iPr BIC). IR (ATR, cm^{-1}): 2107 (C≡C). Anal. calcd for C$_{58}$H$_{76}$**Au$_2$**N$_4$S: C, 55.50; H, 6.10; N, 4.46; S, 2.55; found = C, 54.44; H, 6.13; N, 4.23; S, 2.34. HRMS C$_{58}$H$_{76}$**Au$_2$**N$_4$S theoretical [M − H]$^+$ = 1255.5194; HRMS APCI(ASAP) = 1255.5191. TGA C$_{58}$H$_{76}$**Au$_2$**N$_4$S: T_d = 321.8 °C.

OLED device fabrication and characterisation. For the fabrication of OLED devices, ITO coated substrates (∼15 Ω cm^{-2}) were cleaned with acetone and isopropyl alcohol, and then O_2 plasma treatment was applied to align the energy level with a hole transporting layer. All layers, including organic layers and a LiF/aluminium cathode, were thermally deposited in a high vacuum (∼10^{-7} Torr). The performance of the OLED devices was measured using a Keithley 2635 source-meter and a calibrated Si photodiode. The EL spectra were recorded using an Ocean Optics Flame spectrometer. External quantum efficiencies were calculated by measuring on-axis irradiance and assuming a Lambertian emission profile. The transient EL characteristics are recorded using a spectrometer setup (Andor SR303i) with an electrically gated ICCD camera (AndoriStar DH740 CCI-010). The voltage pulse was obtained using a Keithley 2401 function generator (20 000 Hz frequency and 10 μs pulse width) to collect transient electroluminescence.

Author contributions

13552 | *J. Mater. Chem. C*, 2024, **12**, 13545–13554

This journal is © The Royal Society of Chemistry 2024

photoluminescence studies. M. B. D., N. G. and A. S. R. planned the project and designed the experiments. N. L. P. and M. L. performed theoretical calculations and analyzed theoretical data. A. S. R. wrote the manuscript. All authors contributed to the discussion of the results and analysis of the data, and reviewed and commented on the manuscript.

Data availability

The data supporting this article have been included as part of the ESI.†

Conflicts of interest

There are no conflicts to declare.

Acknowledgements

Notes and references

1 (a) D. A. Parthenopoulos and P. M. Rentzepis, *Science*, 1989, **249**, 843; (b) J. H. Strickler and W. W. Webb, *Opt. Lett.*, 1991, **16**, 1780; (c) B. H. Cumpston, S. P. Ananthavel, S. Barlow, D. L. Dyer, J. E. Ehrlich, L. L. Erskine, A. A. Heikal, S. M. Kuebler, I. Y. S. Lee, D. McCord-Maughon, J. Qin, H. Röckel, M. Rumi, X. L. Wu, S. R. Marder and J. W. Perry, *Nature*, 1999, **398**(6722), 51; (d) Y. Gao, Y. Qu, T. Jiang, H. Zhang, N. He, B. Li, J. Wu and J. Hua, *J. Mater. Chem. C*, 2014, **2**, 6353.

2 (a) M. Charlot, N. Izard, O. Mongin, D. Riehl and M. Blanchard-Desce, *Chem. Phys. Lett.*, 2006, **417**(4–6), 297; (b) R. Westlund, E. Malmström, C. Lopes, J. Öhgren, T. Rodgers, Y. Saito, S. Kawata, E. Glimsdal and M. Lindgren, *Adv. Funct. Mater.*, 2008, **18**, 1939; (c) A. Purc, K. Sobczyk, Y. Sakagami, A. Ando, K. Kamada and D. T. Gryko, *J. Mater. Chem. C*, 2015, **3**, 742; (d) S. Pascal, S. David, C. Andraud and O. Maury, *Chem. Soc. Rev.*, 2021, **50**, 6613.

3 (a) W. Denk, J. J. Strickler and W. W. Webb, *Science*, 1990, **248**, 73; (b) A. Vaziri, J. Tang, H. Shroff and C. V. Shank, *Proc. Natl. Acad. Sci. U. S. A.*, 2008, **105**, 20221; (c) Y. Chen, R. Guan, C. Zhang, J. Huang, L. Ji and H. Chao, *Coord. Chem. Rev.*, 2016, **310**, 16; (d) C. Jin, F. Liang, J. Wang, L. Wang, J. Liu, X. Liao, T. W. Rees, B. Yuan, H. Wang, Y. Shen, Z. Pei, L. Ji and H. Chao, *Angew. Chem., Int. Ed.*, 2020, **59**, 15987; (e) G. Prévot, T. Bsaibess, J. Daniel, C. Genevois, G. Clermont, I. Sasaki, S. Marais, F. Couillaud, S. Crauste-Manciet and M. Blanchard-Desce, *Nanoscale Adv.*, 2020, **2**(4), 1590; (f) M. Rosendale, J. Flores, C. Paviolo, P. Pagano, J. Daniel, J. Ferreira, J. B. Verlhac, L. Groc, L. Cognet and M. Blanchard-Desce, *Adv. Mater.*, 2021, **33**(22), 2006644.

4 (a) J. D. Bhawalkar, N. D. Kumar, C. F. Zhao and P. N. Prasad, *J. Clin. Laser Med. Surg.*, 1997, **15**, 201; (b) M. Drobizhev, N. S. Makarov, S. E. Tillo, T. E. Hughes and A. Rebane, *Nat. Methods*, 2011, **8**(5), 393; (c) J. Schmitt, V. Heitz, A. Sour, F. Bolze, H. Ftouni, J.-F. Nicoud, L. Flamigni and B. Ventura, *Angew. Chem., Int. Ed.*, 2015, **54**, 169; (d) Y. Wang, X. Shi, H. Fang, Z. Han, H. Yuan, Z. Zhu, L. Dong, Z. Guo and X. Wang, *J. Med. Chem.*, 2022, **65**(11), 7786; (e) I. Sasaki, F. Brégier, G. Chemin, J. Daniel, J. Couvez, R. Chkair, M. Vaultier, V. Sol and M. Blanchard-Desce, *Nanomaterials*, 2024, **14**(2), 216.

5 M. Göpper-Maier, *Ann. Phys.*, 1931, **9**(3), 273.

6 (a) M. Rumi, S. Barlow, J. Wang, J. W. Perry and S. R. Marder, *Adv. Polym. Sci.*, 2008, **213**(1), 1; (b) R. L. Roberts, T. Schwich, T. C. Corkery, M. P. Cifuentes, K. A. Green, J. D. Farmer, P. J. Low, T. B. Marder, M. Samoc and M. G. Humphrey, *Adv. Mater.*, 2009, **21**, 2318.

7 (a) J. Olesiak-Banska, M. Gordel, R. Kolkowski, K. Matczyszyn and M. Samoc, *J. Phys. Chem. C*, 2012, **116**, 13731; (b) J. Olesiak-Banska, M. Waszkielewicz, P. Obstarczyk and M. Samoc, *Chem. Soc. Rev.*, 2019, **48**, 4087.

8 S. R. Marder, C. B. Gorman, F. Meyers, J. Perry, G. Bourhill, J.-L. Bredas and B. M. Pierce, *Science*, 1994, **265**, 632.

9 (a) A. Rebane, M. Drobizhev, N. S. Makarov, E. Beuerman, J. E. Haley, D. M. Krein, A. R. Burke, J. L. Flikkema and T. M. Cooper, *J. Phys. Chem. A*, 2011, **115**, 4255; (b) G. S. He, L.-S. Tan, Q. Zheng and P. N. Prasad, *Chem. Rev.*, 2008, **108**, 1245.

10 L. Zhang and M. G. Humphrey, *Coord. Chem. Rev.*, 2022, **473**, 214820.

11 (a) S. K. Hurst, M. P. Cifuentes, A. M. McDonagh, M. G. Humphrey, M. Samoc, B. Luther-Davies, I. Asselberghs and A. Persoons, *J. Organomet. Chem.*, 2002, **642**, 259; (b) S. Goswami, R. W. Winkel and K. S. Schanze, *Inorg. Chem.*, 2015, **54**, 10007; (c) T. R. Ensley, R. M. O'Donnell, J. J. Mihaly, J. E. Haley, T. A. Grusenmeyer and T. G. Gray, *Appl. Opt.*, 2021, **60**, G199.

12 (a) I. R. Whittall, M. G. Humphrey, M. Samoc and B. Luther-Davies, *Angew. Chem., Int. Ed. Engl.*, 1997, **36**(4), 370; (b) A. Moller, P. Bleckenwegner, U. Monkowius and F. Mohr, *J. Organomet. Chem.*, 2016, **813**, 1; (c) K. T. Chan, G. S. M. Tong, W.-P. To, C. Yang, L. Du, D. L. Phillips and C.-M. Che, *Chem. Sci.*, 2017, **8**, 2352; (d) A. Pinto, M. Echeverri, B. Gomez-Lor and L. Rodríguez, *Dyes Pigm.*,

This journal is © The Royal Society of Chemistry 2024

J. Mater. Chem. C, 2024, **12**, 13545–13554 | **13553**

2022, **202**, 110308; (*e*) A. Pinto, M. Echeverri, B. Gomez-Lor and L. Rodríguez, *Dalton Trans.*, 2022, **51**, 8340.

13 (*a*) A. S. Romanov and M. Bochmann, *Organometallics*, 2015, **34**, 2439; (*b*) A. S. Romanov, C. R. Becker, C. E. James, D. Di, D. Credgington, M. Linnolahti and M. Bochmann, *Chem. – Eur. J.*, 2017, **23**(19), 4625; (*c*) A. C. Brannan, H.-H. Cho, A.-P. M. Reponen, M. Linnolahti, M. Bochmann, N. C. Greenham and A. S. Romanov., *Adv. Mater.*, 2024, **36**, 2306249.

14 (*a*) V. Lavallo, Y. Canac, A. DeHope, B. Donnadieu and G. Bertrand, *Angew. Chem., Int. Ed.*, 2005, **44**, 7236; (*b*) E. Tomás-Mendivil, M. M. Hansmann, C. M. Weinstein, R. Jazzar, M. Melaimi and G. Bertrand, *J. Am. Chem. Soc.*, 2017, **139**, 7753; (*c*) F. Chotard, V. Sivchik, M. Linnolahti, M. Bochman and A. S. Romanov, *Chem. Mater.*, 2020, **32**(14), 6114.

15 (*a*) G. Frapper and M. Kertesz, *Inorg. Chem.*, 1993, **32**, 732; (*b*) M. A. Peay, J. E. Heckler, N. Deligonul and T. G. Gray, *Organometallics*, 2011, **30**, 5071.

16 (*a*) D. Y. Kondakov, *Philos. Trans. R. Soc., A*, 2015, **373**, 20140321; (*b*) D. Di, L. Yang, J. M. Richter, L. Meraldi, R. M. Altamimi, A. Y. Alyamani, D. Credgington, K. P. Musselman, J. L. MacManus-Driscoll and R. H. Friend, *Adv. Mater.*, 2017, **29**, 1605987; (*c*) J.-H. Lee, C.-H. Chen, P.-H. Lee, H.-Y. Lin, M.-K. Leung, T.-L. Chiu and C.-F. Lin, *J. Mater. Chem. C*, 2019, **7**, 5874; (*d*) P. Han, C. Lin, E. Xia, J. Cheng, Q. Xia, D. Yang, A. Qin, D. Ma and B. Z. Tang, *Angew. Chem., Int. Ed.*, 2023, **62**, e2023103.

17 (*a*) C. S. Oh, J. Y. Lee, C. H. Noh and S. H. Kim, *J. Mater. Chem. C*, 2016, **4**, 3792; (*b*) S. K. Shin, S. H. Hana and J. Y. Lee, *J. Mater. Chem. C*, 2018, **6**, 10308.

13554 | *J. Mater. Chem. C*, 2024, **12**, 13545–13554

This journal is © The Royal Society of Chemistry 2024